Design of Magneto-Inductive Magnetic Resonance Imaging Catheters

Khoonsake Segkhoonthod, Richard R. A. Syms, *Senior Member, IEEE*, and Ian R. Young

***Abstract*— A catheter-based RF receiver for internal magnetic resonance imaging is described. The device consists of a double-sided thin-film circuit, mounted on a hollow catheter. The system was originally designed for biliary ductal imaging, but is also potentially useful for vascular imaging. Signals are detected using a resonant *L–C* circuit at the catheter tip, transmitted along the catheter using an array of coupled *L–C* resonators, and coupled into a conventional RF system using a demountable inductive transducer. Protection against external B_1 and E fields is obtained by using figure-of-eight-shaped elements with an electrical length shorter than that of an immersed half-wave dipole. Electromagnetic modeling software (AWR Microwave Office) is used to analyze a system designed for ^{1}H imaging at 1.5T, determine the effect of the tissue surround, demonstrate signal detection and transmission and verify intrinsic safety.**

***Index Terms*— Microcoil, magnetic resonance imaging, magneto-inductive waveguide.**

I. Introduction

BECAUSE of their close proximity to the target tissue and restricted field of view for body noise, catheter based RF receivers can offer a significant local signal-to-noise ratio advantage over surface array coils in magnetic resonance imaging (MRI). A wide variety of catheter coils have therefore been developed for arterial imaging [1]–[6], or for tracking of catheter devices [7]–[9]. Despite this advantage, any devices containing conductors (including detection coils and output cables) that are immersed in tissue can induce potentially dangerous RF heating during the excitation phase of MRI.

Firstly, resonant loops may couple directly to the B_1 field of the scanner's RF transmitter. The effect is minimized by the switched insertion of high impedance into the loop during excitation [10], [11]. Secondly, surface waves [12] may be excited on extended lengths of conductor by electric fields, particularly near tuning capacitors in the transmitter coil. If these waves are resonant, the result may be rapid heating [13]–[16]. Unfortunately, the conductors are often closely surrounded by tissue, whose dielectric constant is high at standard clinical frequencies (63.85 MHz for ^{1}H MRI at 1.5 T) [17], so the resonant length is short. Development of decoupling methods to control spurious resonances is more difficult for long conductors. Current approaches include insertion of RF traps [18], [19], transformer segmentation [20], [21] and reversal of conductor directions [22].

We have been studying catheter receiver designs for local MRI of the biliary ductal system. In this case, access may be provided by passing a catheter into the duct through the biopsy channel of a side-opening duodenoscope [23]. A long, smooth, flexible catheter is required, which must also contain a guide wire lumen to assist with cannulation. We have developed flexible thin-film circuits, which can be attached to the outside of a hollow catheter using heat-shrink tubing. Early versions used a printed coil and a coaxial output, while intermediate versions combined a printed coil and a printed cable. The most recent used a printed, transformer-segmented line known as a magneto-inductive (MI) waveguide. The catheters are small and flexible enough for endoscopic delivery, provide an image along their entire length, and are decoupled from both the B_1 and E fields [24]. The approach is general enough to allow the addition of RF detection to many types of catheter.

Development has involved lumped element modeling and iterative experiment. However, the structures are distributed systems immersed in a surrounding medium and subjected to external fields, which cannot easily be described using equivalent circuits. The aim of this paper is therefore to provide a full electromagnetic simulation of signal detection and transmission, especially emphasizing decoupling and safety. MI waveguides and imaging devices are introduced in Section II. Commercial modeling software (AWR Microwave Office) is used to determine the effect of surrounding media in Section III, simulate signal detection and transmission in Section IV, and verify decoupling from external fields in Section V. Conclusions are presented in Section VI.

II. Magneto-Inductive Imaging Catheters

In this section we briefly review the properties of magneto-inductive waveguides and MRI detectors, using low-frequency lumped element circuit theory.

A. Magneto-Inductive Waveguides

MI waveguides are linear arrays of magnetically coupled low-frequency *L-C* resonators with internal resistances R as shown in Fig. 1(a) [25].

Assuming nearest neighbour interaction, the resonators are coupled together by mutual inductance M. For an infinite guide, the currents I_{n-1}, I_n and I_{n+1} at angular frequency ω are related using the recurrence relation:

$$(R + j\omega L + 1/j\omega C)I_n + j\omega M(I_{n-1} + I_{n+1}) = 0 \quad (1)$$

Manuscript received October 8, 2013; revised December 17, 2013; accepted December 23, 2013. Date of publication January 2, 2014; date of current version March 18, 2014. The associate editor coordinating the review of this paper and approving it for publication was Prof. Octavian Postolache.

The authors are with the Electrical and Electronics Engineering Department, Imperial College London, London SW7 2AZ, U.K. (e-mail: k.segkhoonthod09@imperial.ac.uk; r.syms@imperial.ac.uk; youngimarl@aol.com).

Digital Object Identifier 10.1109/JSEN.2013.2296852

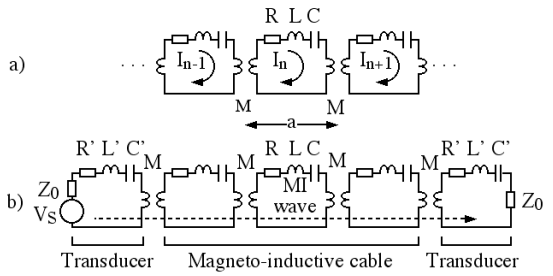

Fig. 1. Lumped element model of (a) infinite magneto-inductive waveguide and (b) finite link between systems with real impedance Z_0.

Assumption of wave solutions $I_n = I_0 \exp(-jnka)$, where I_0 is the wave amplitude, k the propagation constant and a the period, leads to the dispersion relation:

$$1 - \omega_0^2/\omega^2 - j/Q + \kappa cos(ka) = 0 \tag{2}$$

Here, $\omega_0 = 1/\sqrt{(LC)}$ is the angular resonant frequency and $Q = Q_0\omega/\omega_0$, where $Q_0 = \omega_0 L/R$ is the quality factor. Generally the propagation constant is complex. Writing $k = k' - jk''$ and assuming that k'' is small, one obtains:

$$\begin{aligned}(1 - \omega_0^2/\omega^2) + \kappa \cos(k'a) = 0\\ k''a = 1/\{\kappa Q \sin(k'a)\}\end{aligned} \tag{3}$$

The upper equation is the dispersion relation for loss-less MI waves. For positive κ, propagation is allowed only over the frequency band $1/\sqrt{(1+\kappa)} \le \omega/\omega_0 \le 1/\sqrt{(1-\kappa)}$. $k'a$ tends to zero and π at the lower and upper band edges. The effect of finite Q-factor is to introduce loss and allow out-of-band propagation. The lower equation is the approximate loss variation. Loss is minimized at resonance (when $k'a \approx \pi/2$) and inversely proportional to both κ and Q_0. The characteristic impedance is $j\omega M \sin(ka)$, which for low loss reduces approximately to the real value $Z_{0M} = \omega_0 M$ at resonance.

MI waveguides have been demonstrated experimentally, but it has been difficult to achieve good performance. Low propagation loss requires resonators with high Q-factors that are strongly coupled to next neighbours. Small variations in the mutual inductance cause reflection. However, stability is achieved using a thin-film cable that can be flexed without changing M [26]. Practical operation also requires transducers for coupling to RF systems with real impedance Z_0. These can be realized using additional resonant loops with parameters R', L' and C' as shown in Fig. 1(b). Provided $Z_{0M} = Z_0$, efficient power transfer can be achieved over most of the MI band if $L' = L/2$ and $C' = 2C$. Matching may still be achieved if $Z_{0M} \neq Z_0$, but only over a narrow range. Finally, stray capacitance between overlaid elements leads to electric coupling, introducing unwanted high frequency propagation [27].

B. Magneto-Inductive Detectors

Fig. 2 shows a magneto-inductive receiver, which consists of a MI waveguide that is impedance matched to the scanner at one end and self-terminating at the other. The parameters L and C are chosen so that ω_0 is the Larmor frequency. At this

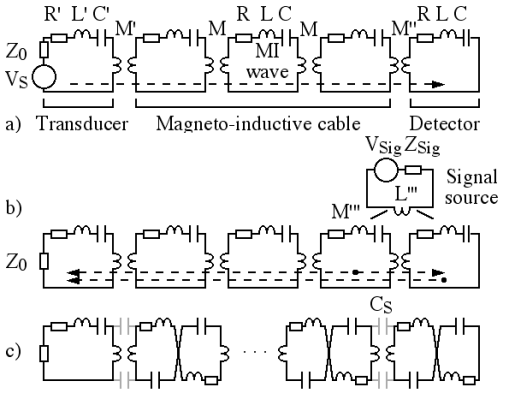

Fig. 2. Lumped element models to demonstrate (a) impedance matching, (b) imaging, and (c) figure-of-eight elements with spurious capacitance.

frequency, Z_{0M} will not always correspond to the scanner's impedance Z_0. However, matching can be achieved using a transducer loop, which in general contains inductance L' and capacitance C' and is also resonant at ω_0. The transducer is coupled to the waveguide via mutual inductance M', and matching is achieved when $\omega_0^2 M'^2 = Z_0 Z_{0M}$. Self-termination is achieved by adjusting the mutual inductance M'' between the final element and the detector so that $\omega_0^2 M''^2 = RZ_{0M}$. In this case, a signal V_S generated by the scanner will excite a MI wave that travels down to the detector without reflection as shown in Fig. 2(a). Conversely, a signal in the detector loop will excite a wave that travels back to the scanner.

MR signals will of course be magnetically induced. This process may be represented as shown in Fig. 2(b). Here a small loop with impedance Z_{sig} containing a voltage V_{sig} models a group of precessing dipoles. The signal may couple to any of the receiver elements. Because of this, the receiver can act as a detector along its entire length. Depending on the arrangement, the signal may couple to more than one element. In the example here, the signal couples to the detector and the final waveguide element via a mutual inductance M''. Several waves are therefore excited. The wave excited in the detector travels to the scanner input as before. However the voltage induced in the waveguide element generates two counter-propagating waves. One travels to the scanner input, while the other is absorbed in the detector. Thus, in general, the detection process is relatively complex.

C. Intrinsic Safety

Further modifications are required to introduce intrinsic safety. Firstly, the resonators must be prevented from coupling directly to B_1 fields. The use of segmentation and the need for catheter integration make it difficult to apply conventional methods based on impedance switching. However, because B_1 fields are generally uniform, some inherent decoupling can be provided by twisting each element into a figure of-eight shape as shown in Fig. 2(c), so that any voltages induced in the two halves cancel. Secondly, the line must be prevented from coupling to external E-fields. The frequency of the ν^{th} order resonance of a length d of conductor should lie at:

$$f_\nu = \nu c/(2d\sqrt{\varepsilon_r}) \tag{4}$$

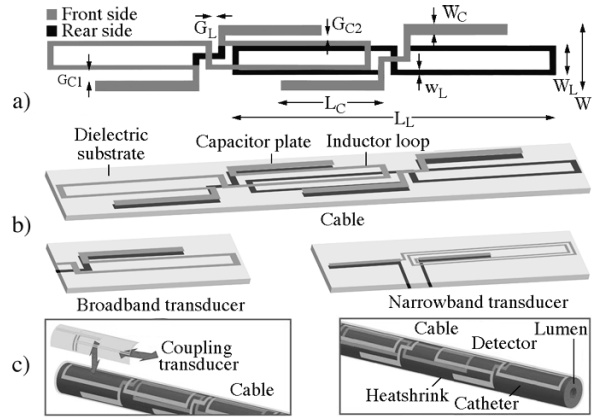

Fig. 3. Thin-film detector: (a) and (b) circuit, and (c) integration on catheter.

Here ν is an integer, c is the velocity of light, and ε_r is the effective relative permittivity of the surround. Assuming that $\varepsilon_r = 77$ (a representative value for tissue), f_1 will lie at 63.85 MHz when $d \approx 27$ cm [18]. The line should therefore be subdivided into lengths shorter than this value. However, even then, there may be a spurious capacitance C_S between sections as shown in Fig. 2(c), which reduces the effect of segmentation. C_S is reduced by avoiding exact overlay of the windings. However, the price is a reduction in magnetic coupling, which from (3) translates into an increase in loss.

D. Thin-Film Realization

The circuit in Fig. 2(c) can be realized in thin-film form using copper-clad polyimide patterned using double-sided exposure and etching. Fig. 3(a) shows a suitable layout. Each inductor is formed in one layer of metal using a track of width w_L, as a figure-of-eight shape of length L_L and width W_L. However, the capacitors are divided into two series-connected components of length L_C and width W_C that use the substrate as an interlayer. The inductors from adjacent elements occupy different sides of the substrate, so that they may be overlaid with their nearest neighbours, but are offset to minimize C_S.

Fig. 3(b) shows three-dimensional representations of the resulting cable, together with a broadband transducer (a halved cable element) and a narrow-band transducer (a two-turn spiral inductor made resonant with a pair of integrated capacitors). The former may be used when $Z_{0M} \approx Z_0$, and the latter when $Z_{0M} \neq Z_0$ and larger mutual inductance is required. A complete detector consists of N elements of MI cable, with one similar element (whose position is chosen to provide self-termination) forming the detector. The circuit is mounted on a hollow catheter as shown in Fig. 3(c). The transducer is demountable, allowing M' to be varied mechanically.

To pass a biopsy channel, the catheter diameter must be small, typically ≈ 3 mm. To allow sufficient flexibility, the conductor and dielectric layers must be thin. Suitable performance has been obtained using 35 μm Cu on 25 μm polyimide [24]. The overall width W of the circuit must be less than the circumference of the scaffold, with the inductor width W_L chosen to place the long conductors on either side of a diameter. The capacitor width W_C must then be adjusted to fit the capacitors into the remaining space. Gaps G_{C1} and G_{C2} are needed to avoid further parasitic capacitance. The lengths L_L and L_C of the inductors and capacitors must yield the correct resonant frequency, and the conductor width w_L must ensure a high Q-factor. The length L_L of each section must be less than the critical resonant length. The number of elements should yield a total length $(N+2)\ L_L/2$ sufficient to pass through a duodenoscope (ca 2 m). Suitable dimensions for catheters operating at 63.8 MHz are summarized in Table I.

TABLE I
DIMENSIONAL PARAMETERS IN FIG. 3 USED IN THE SIMULATIONS

Parameter	Actual value	Model value
W(mm)	7.75	6.75
W_L (mm)	5.00	4.00
W_C (mm)	0.75	0.75
w_C (mm)	0.50	0.50
L_L (mm)	196.50	196.50
L_C (mm)	49.25	49.25
G_{C1} (mm)	0.875	0.875
G_{C2} (mm)	0.375	0.375
G_L (mm)	0.50	0.50

III. MODELING OVERVIEW, AND CLADDING MATERIALS

To reduce run-times, it was assumed that the circuit is entirely flat (rather mounted on a catheter, or bent as in cannulation), thus avoiding the need for full 3D simulation. Modeling was also carried out using a reduced number (7) of elements in the MI cable. These assumptions allow rapid exploration of layouts, while yielding realistic results. Simulation was carried out with commercial electromagnetic analysis software (Microwave Office, AWR Corp., El Segundo, CA, USA), using the Axiem 3D planar method-of-moments solver.

A. AWR Microwave Office

Axiem assumes a multilayer structure for computation. Initially, four-layer structures containing a single metal layer capable of defining simple wires were modeled, as shown in Fig. 4(a). Here, layers 1 and 5 are assumed to be uniform polyolefin, with thickness t_1 and t_5 and complex relative permittivity $\varepsilon_{rC} = \varepsilon'_{rC}$ - $j\varepsilon''_{rC}$. The former mimics the catheter scaffold and the latter the heat-shrink. Layer 2 is assumed to be metal, with thickness t_2 and conductivity σ, and patterned to define an in-plane conductor layout. To allow modeling of tissue immersion, layer 6 was assumed to be a layer of tissue, with thickness t_6 and complex relative permittivity $\varepsilon_{rT} = \varepsilon'_{rT}$ - $j\,\varepsilon''_{rT}$.

Six-layer structures containing a second metal layer to allow definition of a full circuit were then investigated, as shown in Fig. 4(b). Here layer 3 is assumed to be a uniform polyimide interlayer, with thickness t_3 and relative permittivity $\varepsilon_{rI} = \varepsilon'_{rI}$ - $j\varepsilon''_{rI}$. Layer 4 is assumed to be metal, with thickness t_4 and conductivity σ, and may be patterned to define a separate conductor layout. Finally, once the effect of

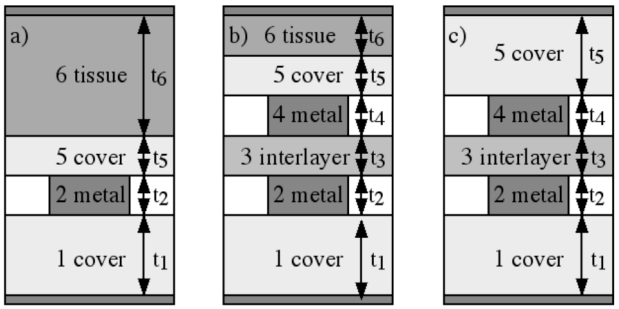

Fig. 4. (a) Plastic-embedded single-layer metal, with tissue layer. (b) and (c) Plastic-embedded double-layer metal, with and without tissue.

TABLE II
MATERIAL PARAMETERS USED IN THE SIMULATIONS

Material	Conductivity σ (S/m)	
Copper	2.96 x 10^7	
Material	Real permittivity ε_r'	Tan(δ) $\varepsilon_r''/\varepsilon_r'$
Polyolefin	2.7	0.06
Polyimide	3.5	0.06
Tissue	77	0

immersion had been established, simpler five-layer structures omitting the tissue were investigated as shown in Fig. 4(c).

Different devices were simulated, by specifying an appropriate metal layout and ports connecting to sources and loads, each of 50 Ω impedance. The assumed values of the material parameters are shown in Table II. Typically, these are as found in the literature, but the conductivity was reduced from the value obtained in bulk copper ($\sigma = 5.96$ x 10^7 S/m) to mimic the relatively poor performance of thin film Cu.

B. Immersed Wires

To begin with, the effect of tissue immersion was simulated using the structure of Fig. 4(a), with the aim of clarifying the effects of a plastic cover on surface waves. The metal pattern was first chosen to define a long wire of width 0.25 mm, with a pair of weakly coupled short dipoles $L_G = 1.65$ mm away from the wire at either end for electrical excitation and detection as shown in Fig. 5(a). Calculation of the frequency variation of transmission (S_{21}) then yielded a response containing resonant peaks, each at a frequency f_ν corresponding to the ν^{th} order resonance of the wire. Knowledge of (say) f_1 then allowed the effective value of ε_r (a weighted average of the permittivity of all the surrounding layers) to be estimated using Equation 4.

The thickness t_1 and t_6 of the polyolefin substrate and tissue were both taken as 30 mm, the thickness t_2 of the copper was 35 μm, and the thickness t_5 of the polyolefin cover was varied. Fig. 5(b) shows the variation of ε_r with t_5. When $t_5 = 0$, a value of $\varepsilon_r = 39.1$ was obtained. This value is almost exactly equal to $(\varepsilon_{r1} + \varepsilon_{r6})/2$, implying that the relative permittivity seen by the wire is the average of the values of the polyolefin support and the tissue surround. However, as t_5 increases, ε_r falls towards 2.7, the value for

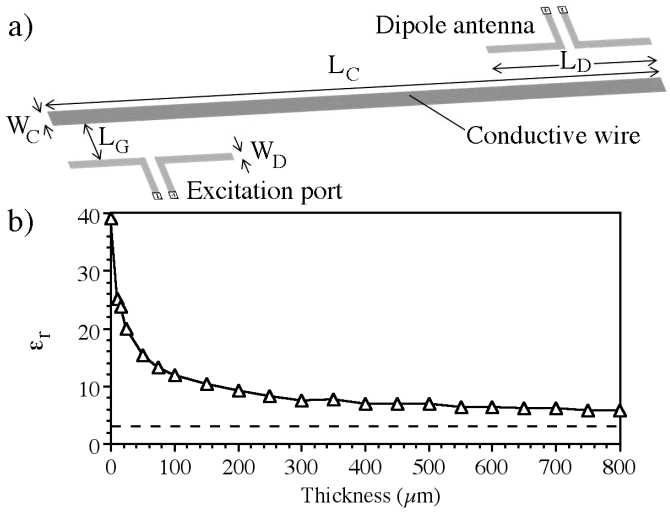

Fig. 5. (a) Layout used for simulation of immersed wires. (b) Variation of effective relative dielectric constant with cover layer thickness.

complete immersion in polyolefin. The initial rapid reduction in ε_r implies that even a thin cover is sufficient to reduce the wavelength-shortening effect of surrounding tissue significantly. Consequently, designs based on full immersion in tissue and implemented with (say) a 250 μm thick heat-shrink tube will be extremely conservative.

C. Parasitic Capacitance

The origin of the parasitic capacitance C_S, and the effect of tissue immersion on C_S, was then simulated using the double-layer metal structure of Fig. 4(b). The thickness of the additional layers were $t_3 = 25$ μm (polyimide interlayer) and $t_4 = 35$ μm (second Cu layer). Fig. 6(a) shows a typical arrangement. Here, conductors on the two layers have been offset to avoid parallel-plate effects, but electric coupling is still obtained through fringing fields that penetrate multiple layers of dielectric. As a result, C_S may be large if significant field exists in the tissue, which has a high dielectric constant. Problems of this type are important in multilayer VLSI circuits. Unfortunately, analytic evaluation of the capacitance is extremely difficult. Solutions for infinite, asymmetrically placed strips in uniform dielectrics have been obtained using conformal mapping [28], and similar approaches have been adopted for more complex geometries [29]. However, the problem must generally be tackled numerically.

Here, we have determined the parasitic capacitance using a resonant circuit based on two U-shaped metallic loops provided on the two available metal layers as shown in Fig. 6(b). The right-hand part of the circuit defines an inductor, whose value may be determined using a known capacitance, while the left-hand part defines two series-connected parasitic capacitors. The circuit response is probed using ports attached to the capacitors, and their value is extracted from the resonant frequency. Fig. 6(c) shows the variation of C_S with the cover layer thickness t_5. Once again, C_S falls rapidly from an initial value C_{S0} when $t_5 = 0$, stabilizing when t_5 rises to a few hundred microns at the value obtained for an infinitely thick cladding. We may therefore deduce that a plastic heat-

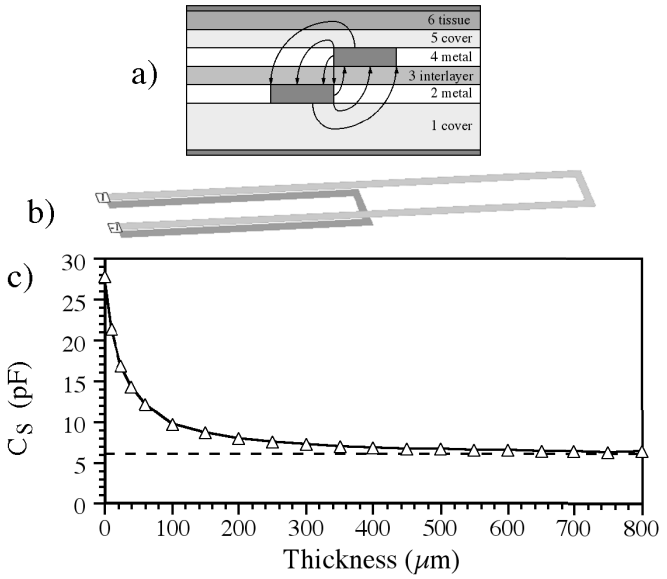

Fig. 6. (a) Origin of electric coupling. (b) Layout for simulation of parasitic capacitance. (c) Variation of C_S with cover layer thickness.

shrink also provides an effective shield against the effect of surrounding tissue on fringing fields. Further simulations were therefore carried out using the layer structure of Fig. 4(c), which omits the tissue layer entirely, and instead assumes a 30 mm thick layer of polyolefin above the circuit.

IV. Signal Transmission and Detection

We now consider specific circuits of the type shown in Fig. 3. Layout dimensions largely follow those of the experimental devices given in Table I, but with some small differences. Particularly, 2D simulation of 3D inductors meant that exactly corresponding values of self- and mutual inductance could not be obtained simply by adopting the same inductor width, and slightly modified values were therefore used. These were obtained by trial-and-error, and are as detailed in Table I.

A. Single and Coupled Resonant Elements

The analysis of Sec. II implies that the properties of MI waveguides largely follow from the resistance R, inductance L and capacitance C of a single element and the mutual inductance M. Their effect on dispersion and loss can be summarized in terms of the angular resonant frequency $\omega_0 = 1/\sqrt{(LC)}$, the coupling coefficient $\kappa = 2M/L$ and the Q-factor $Q_0 = \omega_0 L/R$. Approximate values of ω_0, κ and Q_0 were known from comparisons between experimental data and MATLAB models of the circuits in Figs. 1 and 2. Equivalent values were established in AWR using techniques that mimic experimental methods.

Two simple AWR layouts were first defined as shown in Fig. 7(a). The upper one is a single resonant element, interrogated inductively using two weak taps. The lower one is a pair of coupled resonant elements, again interrogated inductively. Simulation of the frequency variation of transmission through the upper layout allowed the resonant frequency $f_0 = \omega_0/2\pi$ and the quality factor Q_0 of a single element

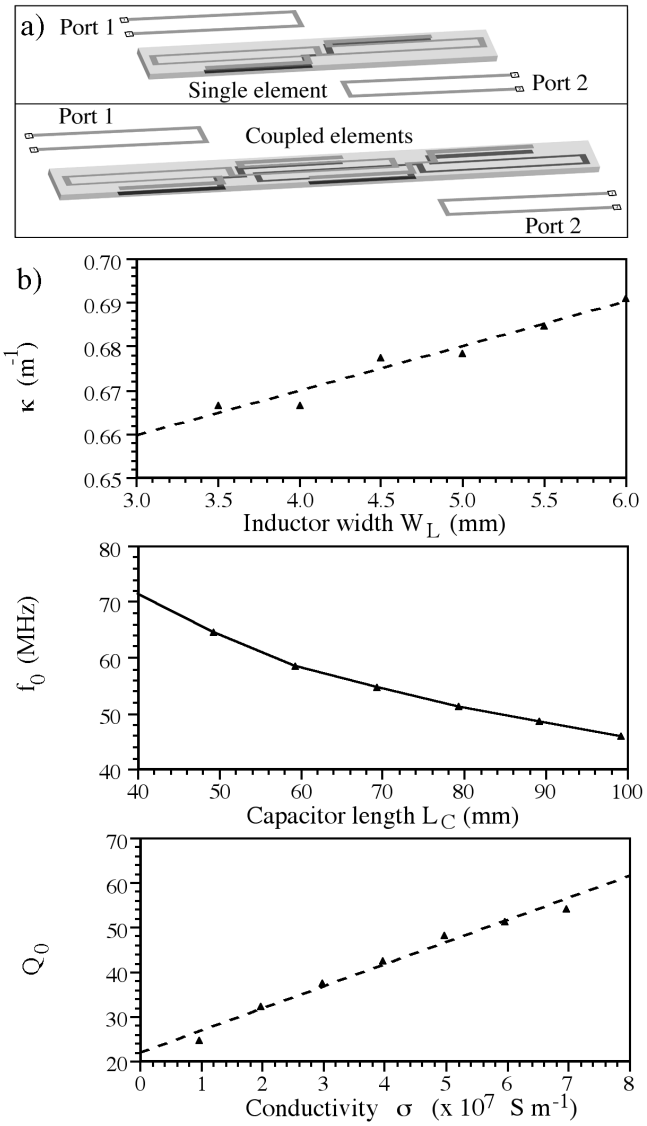

Fig. 7. Parameter extraction. (a) AWR models. (b) Variation of κ with W_L, f_0 with L_C and Q_0 with σ.

to be found from the position and 3 dB bandwidth of the resonance. Similarly, simulation of the lower layout allowed the two resonant frequencies $f_1 = 1/\{2\pi\sqrt{[(L+M)C]}\}$and $f_2 = 1/\{2\pi\sqrt{[(L-M)C]}\}$inherent in a coupled system to be identified. These values allowed the coupling coefficient to be estimated as $\kappa = 2\{f_2^2/f_1^2 - 1\}/\{f_2^2/f_1^2 + 1\}$.

In each case, the inductor width W_L and the capacitor length L_C were initially assumed to have the experimental values, and the conductivity to have the value for bulk copper. The inductor width W_L was first adjusted to obtain the correct value of κ. The capacitor length L_C was then adjusted to obtain the correct value of f_0. Finally, the conductivity was adjusted to obtain the correct Q-factor.

Simulations were carried out using air and polyolefin as surrounds. In contrast to the previous section on electric effects, little difference was obtained in the parameter values of the components (whose behaviour is dominated by magnetic effects). Fig. 7(b) shows the variations of κ, f_0 and Q_0 with W_L, L_C and σ, and Table III details the final values.

TABLE III
PERFORMANCE PARAMETERS OF MI WAVEGUIDES

Parameter	κ	f_0	Q_0
Value	0.684	63.90	40.96

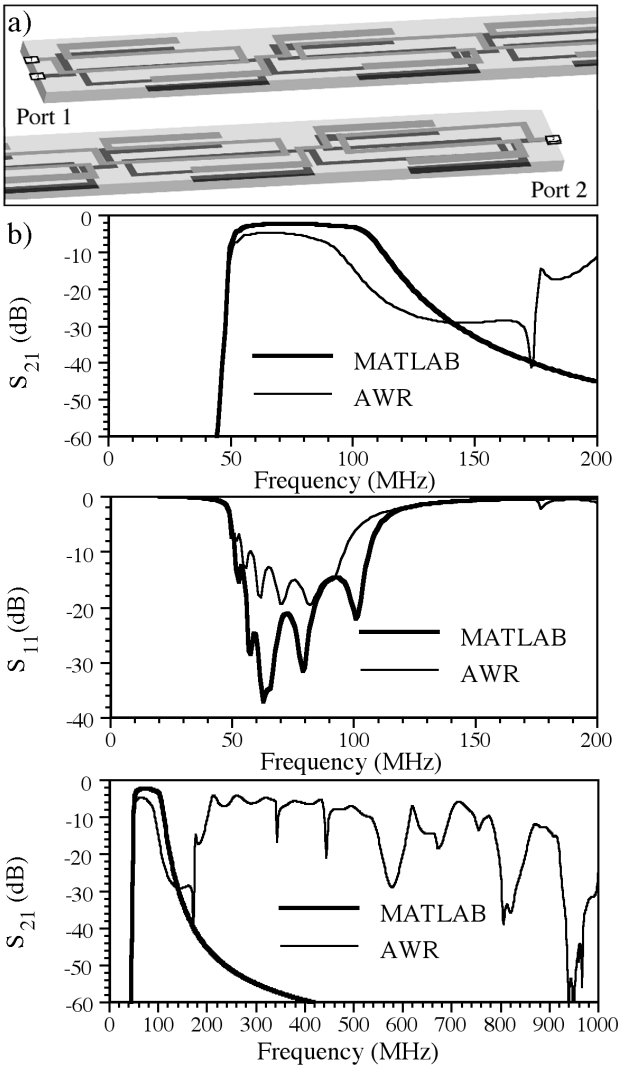

Fig. 8. Cable link simulation. (a) AWR model. (b) Frequency variations of S_{21} and S_{11} predicted by AWR and MATLAB, over different frequency ranges.

B. Complete Magneto-Inductive Systems

Complete links could then be simulated. For example, Fig. 8(a) shows an AWR model equivalent to Fig. 1(b). Here a length of cable is connected at either end to input and output ports using halved cable elements acting as a broadband transducers.

Fig. 8(b) compares the frequency variation of transmission and reflection (S_{21} and S_{11}) predicted using the AWR model and a MATLAB solution of the governing equations for Fig. 1(b). The transmission is low, except in the MI band from 50 MHz to 120 MHz where it reaches around -5 dB. The agreement between the two models is generally good, except at high frequency, where it rises in the AWR model. When

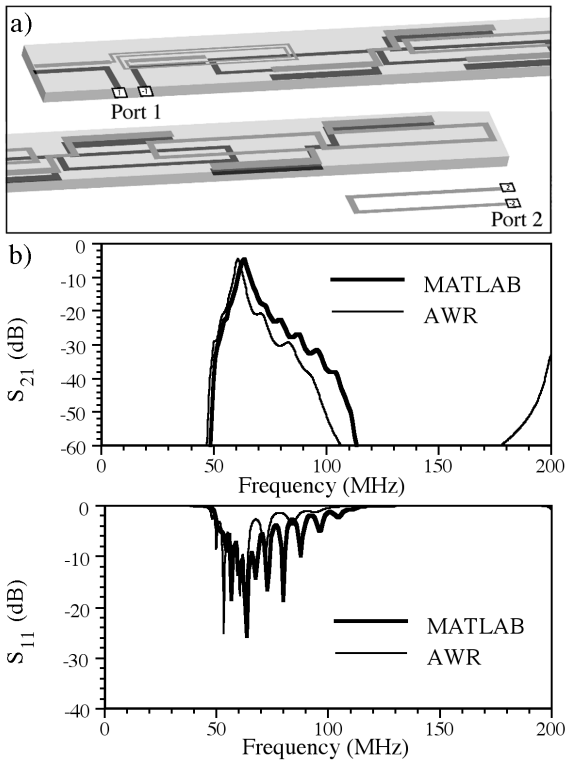

Fig. 9. Detector simulation. (a) AWR model. (b) Frequency variations of S_{11} and S_{21} as predicted by AWR and MATLAB.

the same data is plotted over an extended frequency range, it is clear that this effect can be attributed to an additional propagation band in the AWR model, which is not predicted using the simple MI waveguide model. This band is due to parasitic capacitance between closely spaced tracks where the inductors are overlaid to achieve strong magnetic coupling, and has the additional effect of reducing the width of the MI band somewhat [27]. The predicted pass-band is reduced from 50-105 MHz to 50-75 MHz, and the predicted loss at 63.85 MHz is increased by 3 dB. Similarly, the reflection is generally high except in the MI band. For both models, $S_{11} \approx$ -20 dB over a reasonable frequency range, indicating that broadband impedance matching has been achieved.

Complete magneto-inductive detectors could then be simulated. For example, Fig. 9(a) shows an AWR model equivalent to Fig. 2(b). Here a length of cable is connected at one end to an input port using a spiral resonant inductor, which acts as a narrow-band transducer, and at the other end using an element whose position is adjusted to form a matched termination. A weak inductive tap is also provided, to allow transmission to be simulated. In this case, additional dimensional adjustments were required to achieve the correct electrical parameters. The lengths of the capacitors in the transducer were first chosen to set the resonance correctly. The positions of the transducer and detector were then adjusted to achieve impedance matching at either end.

Fig. 9(b) shows the frequency variation of S_{21} and S_{11} predicted using the AWR model and a MATLAB solution of the governing equations for Fig. 2(b). In the former case, the data were offset by a fixed amount to compensate for the use

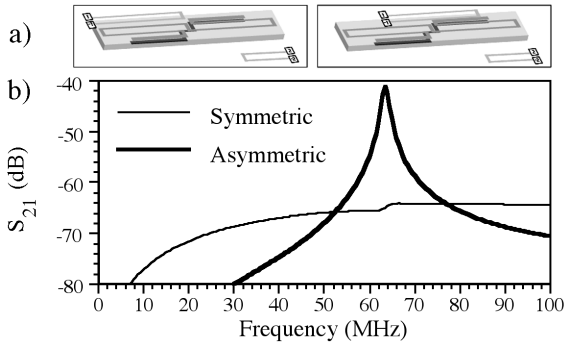

Fig. 10. Simulation of magnetic decoupling. (a) AWR models. (b) Frequency variations of S_{21} for asymmetric and symmetric excitation.

of a weak tap for sampling. The agreement between the two models is again good. There is again transmission over the MI band, but signal now peaks sharply at the resonant frequency indicating that the system is now functioning as a resonant detector with a Q-factor of ≈ 40. The predicted pass-band is again reduced as described with reference to Fig. 8. There is also a slight detuning of the resonant peak (by 3 MHz), which would in practice require mechanical tuning of the detector element. For both models, $S_{11} \approx -20$ dB near the resonant frequency, indicating that narrow-band impedance matching has been achieved.

V. Decoupling from External Fields

We now consider decoupling from external fields. Additional structures are required to generate suitable B_1 and E fields and detect the resulting response.

A. Magnetic Fields

For magnetic fields, external excitation and detection can be carried out using inductive loops as shown in Fig. 10(a). In the left-hand diagram, an offset loop on the left-hand side is used to excite a single resonant element of the magneto-inductive cable, and a similar loop on the right-hand side is used to detect any current flowing as a result of magnetic induction. In this case the excitation is asymmetric, and the frequency variation of the transmission S_{21} between the loops displays a pronounced resonance at 63.85 MHz, as shown in Fig. 10(b). In the right-hand diagram in Fig. 10(a), the excitation loop is now placed centrally. In this case the excitation is symmetric, and the resonance is largely absent in the corresponding frequency variation in Fig. 10(b) due to cancellation of the induction. The figure-of-eight layout therefore provides protection against balanced external magnetic fields, but not unbalanced fields.

B. Electric Fields

For electric fields, external excitation and detection can be carried out using antennas as shown in Fig. 11(a). Excitation was carried out using a short (a tenth of a wavelength long) dipole at the left-hand end of the structure, a distance of 12.5 mm beneath. Detection of any excited currents was carried out using a similar dipole placed at the right-hand

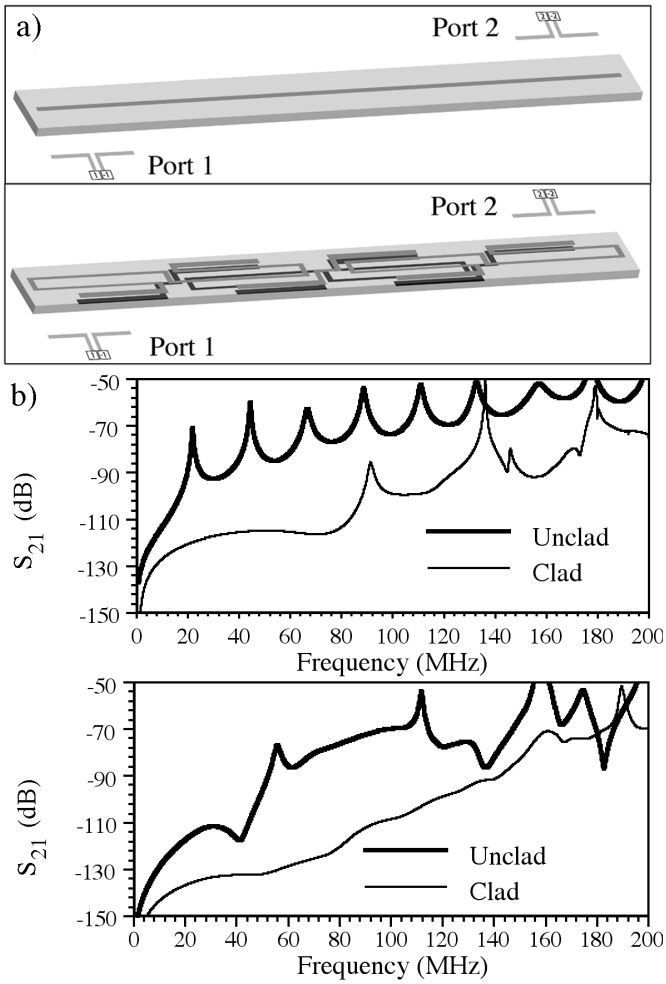

Fig. 11. Simulation of electric decoupling. (a) AWR models. (b) Frequency variations of S_{21} for wire and cable, with and without cladding.

end, 12.5 mm above. Two structures were compared: an undivided wire of width 2.0 mm and thickness 0.35 μm (upper diagram) and a magneto-inductive cable (lower diagram), in each case of length corresponding to 7 cable sections. Simulations were carried out with the structure under test covered with a dielectric of relative permittivity $\varepsilon_r = 77$, firstly with no cladding at all and secondly with a 30 mm polyolefin lower cladding and a 250 μm thick polyolefin upper cladding. The upper diagram in Fig. 11(b) shows the frequency variation of transmission S_{21} for wires. With no cladding, many resonances can be seen, extending as low as 20 MHz. The effect of the cladding is to decrease the effective permittivity seen by the wire, and significantly increase the frequency of the lowest order resonance.

The lower diagram in Fig. 11(b) shows the corresponding frequency variation for the MI cable. The effect of subdivision is, as expected, to raise the frequency of the lowest order resonance. However, the relatively large value of parasitic capacitance C_S obtained for the unclad system limits the effect of subdivision, so that the lowest order resonance actually lies below 63.85 MHz. The effect of the cladding is simultaneously to decrease the effective permittivity seen by conductors and to reduce C_S. In this case, there are no significant resonances up

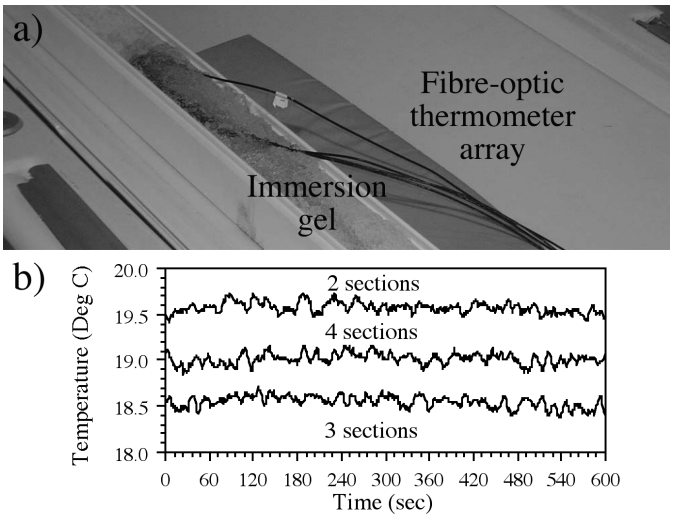

Fig. 12. (a) Arrangement for experimental measurement of RF-induced heating effects. (b) Time evolution of temperature.

to at least 150 MHz, and the attenuation in transmission is very substantial indeed. The segmented arrangement then provides extremely effective protection against external electric fields.

VI. Conclusion

A detailed investigation of the thin-film circuit used in a catheter probe for high-resolution internal imaging has been carried out using commercial software (AWR Microwave Office). The circuit consists of a self-terminating magneto-inductive waveguide, formed from a set of magnetically coupled L-C resonators with inductors and capacitors that are entirely fabricated by double-sided patterning and etching of copper-clad Kapton. The resonant-elements are formed into figure-of-eight loops to provide inherent rejection of external B_1 fields, and the length of each element is chosen to be less than the resonant length of an immersed dipole at the operating frequency to avoid excitation of standing waves by external E fields. The circuit is wrapped around a catheter and sealed in place with heat shrink tubing, and connection to the circuit is made using an inductive coupling transducer. Potential applications include biliary and arterial imaging.

The catheter architecture is an advance on previous internal probe designs, since it leaves the catheter lumen free for use with the guide-wire needed for reliable cannulation in biliary imaging. However, the position of the thin-film circuit leaves it separated from external tissue only by a thin insulation layer. It is therefore important to understand the precise effect of this layer on MRI safety. This investigation represents the first detailed simulation of such external effects.

The numerical simulations verify previous lumped element circuit analysis. Physical dimensions that give suitable component values have been established, subject to known layout constraints and simplification to a flat circuit. Matching between the MI waveguide and the scanner input has been achieved using a transformer, and matching between the final element of the waveguide and the detector by adjusting their separation. Operation of MI links and receivers has been simulated. The effect of parasitic capacitance between resonant elements has been quantified, and shown to allow additional high-frequency pass-bands for differential mode signals. The effect of an external medium has been clarified. The results show clearly that the heat-shrink tubing used to attach the circuit to the catheter scaffold serves the important function of reducing the effective permittivity of the surround and minimizing the value of parasitic capacitances. As a result, the circuit is indeed decoupled from external B_1 and E-fields and intrinsically safe.

High-resolution imaging with experimental catheter receivers has already been described [24]. Preliminary ^{1}H MR safety experiments have also been carried out, using a 1.5T GE Signa Excite scanner. MI cables with 2, 3 and 4 sections were suspended in a viscous gel based on polyacrylic acid and saline designed to mimic human tissue as shown in Fig. 12(a). The temperature was monitored at the cable midpoints and ends with a multi-channel fibre optic temperature probe while scanning with a RF-intensive FIESTA sequence (120^o flip angle, echo time TE $=$ 2.3 ms, repeat time TR $=$ 8 ms) with the cables close to the system body coil. Fig. 12(b) shows the time evolution of the midpoint temperature. Here, differences between probes are attributable to calibration errors. The lack of any temperature rise after 10 minutes RF heating tends to support the simulations presented here. However further work is clearly required to confirm MR safety before *in vivo* use.

References

[1] H. L. Kantor, R. W. Briggs, and R. S. Balaban, "*In vivo* 31P nuclear magnetic resonance measurements in canine heart using a catheter-coil," *Circle Res.*, vol. 55, pp. 261–266, Aug. 1984.

[2] K. Kandarpa, P. Jakab, S. Patz, F. J. Schoen, and F. A. Jolesz, "Prototype miniature endoluminal MR imaging catheter," *J. Vascular Intervent. Radiol.*, vol. 4, pp. 419–427, May/Jun. 1993.

[3] O. Ocali and E. Atalar, "Intravascular magnetic resonance imaging using a loopless catheter antenna," *Magn. Reson. Med.*, vol. 37, pp. 112–118, Jan. 1997.

[4] P. A. Bottomley, E. Atalar, R. F. Lee, K. A. Shunk, and A. Lardo, "Cardiovascular MRI probes for the outside in and for the inside out," *Magn. Reson. Mater. Phys. Biol. Med.*, vol. 11, pp. 49–51, Nov. 2000.

[5] D. Crottet, R. Meuli, S. Wicky, and J. J. van der Kink, "Reciprocity and sensitivity of opposed-solenoid endovascular MRI probes," *J. Magn. Reson.*, vol. 159, pp. 219–225, Dec. 2002.

[6] C. T. Farrar, V. J. Wedeen, and J. L. Ackerman, "Cylindrical meanderline radiofrequency coil for intravascular magnetic resonance studies of atherosclerotic plaque," *Magn. Reson. Med.*, vol. 53, pp. 226–230, Jan. 2005.

[7] M. Burl, G. A. Coutts, D. Herlihy, R. Hill-Cottingham, J. E. Eastham, J. V. Hajnal, *et al.*, "Twisted-pair RF coil suitable for locating the track of a catheter," *Magn. Reson. Med.*, vol. 41, pp. 636–638, Mar. 1999.

[8] Q. Zhang, M. Wendt, A. J. Aschoff, J. S. Lewin, and J. L. Duerk, "A multielement RF coil for MRI guidance of interventional devices," *J. Magn. Reson. Imag.*, vol. 14, pp. 56–62, Jul. 2001.

[9] S. Zuehlsdorff, R. Umathum, S. Volz, P. Hallscheidt, C. Fink, W. Semmler, *et al.*, "MR coil design for simultaneous tip tracking and curvature delineation of a catheter," *Magn. Reson. Med.*, vol. 52, pp. 214–218, Jul. 2004.

[10] J. S. Hyde, R. J. Rilling, and A. Jesmanowicz, "Passive decoupling of surface coils by pole insertion," *J. Magn. Reson.*, vol. 89, pp. 485–495, Oct. 1990.

[11] W. A. Edelstein, C. J. Hardy, and O. M. Mueller, "Electronic decoupling of surface coil receivers for NMR imaging and spectroscopy," *J. Magn. Reson.*, vol. 67, pp. 156–161, Mar. 1986.

[12] G. Goubau, "On the excitation of surface waves," *Proc. IRE.*, vol. 40, no. 7, pp. 865–868, Jul. 1952.

[13] M. K. Konings, L. W. Bartels, H. F. M. Smits, and C. J. G. Bakker, "Heating around intravascular guidewires by resonating RF waves," *J. Magn. Reson. Imag.*, vol. 12, pp. 79–95, Jul. 2000.
[14] C.-Y. Liu, K. Farahani, D. S. K. Lu, G. Duckwiler, and A. Oppelt, "Safety of MRI-guided endovascular guidewire applications," *J. Magn. Reson. Imag.*, vol. 12, pp. 75–78, Jul. 2000.
[15] W. R. Nitz, A. Oppelt, W. Renz, C. Manke, M. Lenhart, and J. Link, "On the heating of linear conductive structures as guidewires and catheters in interventional MRI," *J. Mag. Res. Imag.*, vol. 13, pp. 105–114, Jan. 2001.
[16] S. M. Park, R. Kamondetdacha, A. Amjad, and J. A. Nyenhuis, "MRI safety: RF-induced heating near straight wires," *IEEE Trans. Magn.*, vol. 41, no. 10, pp. 4197–4199, Oct. 2005.
[17] A. Surowiec, S. S. Stuchly, L. Eidus, and A. Swarup, "*In-vitro* dielectric properties of human tissue at radio frequencies," *Phys. Med. Biol.*, vol. 32, pp. 615–621, May 1987.
[18] E. Atalar, "Safe coaxial cables," in *Proc. 7th Ann. Meeting ISMRM*, May 1999, p. 1006.
[19] M. E. Ladd and H. H. Quick, "Reduction of resonant RF heating in intravascular catheters using coaxial chokes," *Magn. Reson. Med.*, vol. 43, pp. 615–619, Apr. 2000.
[20] S. Weiss, P. Vernickel, T. Schaeffter, V. Schulz, and B. Gleich, "Transmission line for improved RF safety of interventional devices," *Magn. Reson. Med.*, vol. 54, pp. 182–189, Jul. 2005.
[21] A. Krafft, S. Müller, R. Umathum, W. Semmler, and M. Bock, "B1 field-insensitive transformers for RF-safe transmission lines," *Magn. Reson. Mater. Phys.*, vol. 19, pp. 257–266, Nov. 2006.
[22] P. A. Bottomley, A. Kumar, W. A. Edelstein, J. P. Allen, and P. V. Karmarkar, "Designing passive MRI-safe implantable conducting leads with electrodes," *Med. Phys.*, vol. 37, pp. 3828–3843, Jul. 2010.
[23] R. Kozarek, "Biliary ERCP," *Endoscopy*, vol. 39, pp. 11–16, Jan. 2007.
[24] R. R. A. Syms, I. R. Young, M. M. Ahmad, S. D. Taylor-Robinson, and M. Rea, "Magneto-inductive catheter receiver for magnetic resonance imaging," *IEEE Trans. Biomed. Eng.*, vol. 60, no. 9, pp. 2421–2431, Sep. 2013.
[25] E. Shamonina, V. A. Kalinin, K. H. Ringhofer, and L. Solymar, "Magneto-inductive waveguide," *Electr. Lett.*, vol. 38, pp. 371–373, Apr. 2002.
[26] R. R. A. Syms, I. R. Young, L. Solymar, and T. Floume, "Thin-film magneto-inductive cables," *J. Phys. D, Appl. Phys.*, vol. 43, p. 055102, Jan. 2010.
[27] R. R. A. Syms and T. Floume, "Electric coupling in strongly coupled magneto-inductive cable," in *Proc. 7th Int. Congr. Adv. Electromagn. Metamater. Microw. Opt.*, Sep. 2013, pp. 1–3.
[28] A. E. H. Love, "Some electrostatic distributions in two dimensions," *Proc. London Math. Soc.*, vol. s2–22, pp. 337–369, Jan. 1924.
[29] A. Bansal, B. P. Paul, and K. Roy, "An analytic fringe capacitance model for interconnects using conformal mapping," *IEEE Trans. Comput. Aided Des. Integr. Circle Syst.*, vol. 25, no. 12, pp. 2765–2774, Dec. 2006.

Khoonsake Segkhoonthod is currently pursuing the Ph.D. degree at the Electrical and Electronic Engineering Department, Imperial College London, U.K., with a particular interest in the development of internal probes for magnetic resonance imaging of cholangiocarcinoma.

Richard R. A. Syms (SM'02) is a Professor of microsystems technology from the Electrical and Electronic Engineering Department, Imperial College London, London, U.K., where he heads the Optical and Semiconductor Devices Group. He has published over 200 journal and conference papers on electromagnetic theory, sensors, metamaterials, and medical imaging. He is a Fellow of the Royal Academy of Engineering, the Institute of Electrical Engineers, and the Institute of Physics.

Ian R. Young is a Senior Research Fellow with the Electrical and Electronic Engineering Department, Imperial College London, U.K. He has published over 300 papers on MRI. His current interests are *in-vivo* MRI and MR-guided surgical robots. He is a Fellow of the Royal Society and the Royal Academy of Engineering, and he received the Gold Medal of SMRM and the Sir Frank Whittle Prize.